01 Jan 2018

A Two-Dimensional Simulation of Grain Structure Growth within Substrate and Fusion Zone during Direct Metal Deposition

Jingwei Zhang

Lei Yan

Wei Li

Frank W. Liou
Missouri University of Science and Technology, liou@mst.edu

Chapter 2

A Two-Dimensional Simulation of Grain Structure Growth within Substrate and Fusion Zone during Direct Metal Deposition

Jingwei Zhang, Lei Yan, Wei Li and Frank Liou

Additional information is available at the end of the chapter

http://dx.doi.org/10.5772/intechopen.73107

Abstract

In this chapter, a predictive multiscale model based on a cellular automaton (CA)-finite element (FE) method has been developed to simulate thermal history and microstructure evolution during metal solidification for direct metal deposition (DMD) process. The macroscopic FE calculation that is validated by the thermocouple experiment is developed to simulate the transient temperature field and cooling rate of single layer and multiple layers. In order to integrate the different scales, a CA-FE coupled model is developed to combine with thermal history and simulate grain growth. In the mesoscopic CA model, heterogeneous nucleation sites, grain growth orientation and rate, epitaxial growth, remelting of preexisting grains, metal addition, grain competitive growth and columnar to equiaxed phenomena are simulated. The CA model is able to show the entrapment of neighboring cells and the relationship between undercooling and the grain growth rate. The model predicts the grain size and morphological evolution during the solidification phase of the deposition process. The developed "decentered polygon" growth algorithm is appropriate for the nonuniform temperature field. Finally, the single- and multiple-layer DMD experiments are conducted to validate the characteristics of grain features in the simulation.

Keywords: finite element, cellular automata, grain morphology, direct metal deposition, thermal modeling

1. Introduction

Compared with the conventional subtractive manufacturing technologies, additive manufacturing (AM) has unique advantages including low heat input, small heat-affected zone, solid-free-form fabrication, near-net-shape and so on. Direct metal deposition (DMD), a rapid developing AM

technique, is able to manufacture a fully dense metal part without intermediate steps, which is especially appropriate for the heterogeneous components manufacturing. During the deposition process, solidification thermodynamics determined by a series of process parameters affect microstructure evolution, which directly affects materials' mechanical properties. The temperature field history and the cooling rate are the key factors to control the solidification microstructure after DMD process [1]. Several approaches, including stochastic and deterministic, have been taken to model solidification microstructure evolution. Anderson and Srolovitz et al. [2, 3] developed a Monte Carlo (MC) stochastic method to simulate the grain growth, grain size distribution, curvature and growth rate as well as their interrelationships. Saito and Enomoto [4] incorporated the anisotropy of the grain boundary energy, the pinning effect of precipitates on growth kinetics into the MC simulation. Another idea of modeling is the deterministic approach. Chen [5] investigated a phase field (PF) method to model and to predict the mesoscale morphological and microstructure evolution in materials. C.E. Krill III, Böttger B, and Moelans N et al. [6–8] developed PF to simulate 2D grain growth, 3D grain growth and equiaxed solidification. However, a phase field model usually carries a very high computational cost because of a requirement for a particularly fine computational grid.

In order to reduce the computational cost, Rappaz and Gandin [9] put forward a 2D cellular automaton approach to model the grain structure formation in the solidification process. The model includes the mechanisms of heterogeneous nucleation and grain growth during the casting process. Nucleation occurring at the solid/liquid interface and the liquid bulk is treated by using different nucleation sites preference. The crystallographic orientation and locations of the grains are randomly selected among a certain number of orientation classes and millions of CA cells, respectively. However, the model was only applied to uniform temperature field. In order to develop the nonuniform temperature prediction, Gandin and Rappaz [10] proposed a 2D cellular automaton (CA) technique for the simulation of grain formation during solidification. The nonuniform temperature situation was fully coupled to finite element (FE) heat flow calculation with enthalpy. This progress made it possible to combine the temperature field history with the microstructure evolution. The coupled CA-FE model is applied to A1-7 wt% Si alloy. A 3D CA-FE model was analyzed for the prediction of dendritic grain structures formed during solidification [11]. The potentiality of the CA-FE model is demonstrated through the predictions of typical grain structures formed during the investment casting and continuous casting processes. Based on the features of several developing approaches, Choudhury et al. [12] compared a CA model with a PF model for dendritic solidification of an Al-4 wt%Cu alloy, 2D and 3D at different undercooling conditions. In 2D case, there is a very good agreement of the simulated tip properties. At high undercooling, the CA model becomes more favorable, as its reproduction of the theoretical behavior is improved. Since the CA model can simulate at coarse scales during a relatively short time, its output can be employed as the input for a PF simulation in order to resolve finer details of microstructure formation within grains. This can be utilized to build a hybrid model to integrate CA high efficiency and PF accuracy. Dore [13] investigated quantitative prediction of microsegregation during solidification of the ternary alloy system, which is applied to solidification of Al–Mg–Si. Jarvis et al. [14] firstly compared 1D, 2D and 3D cellular automaton finite difference (CA-FD) simulations of nonequilibrium solidification in Al–3.95Cu–0.8Mg ternary alloy. It has been demonstrated that there is a good agreement between all the CA-FD models in terms of primary α-Al phase. However, final dendrite arm spacings of 2D and 3D are slightly overestimated.

High cooling rate and nonequilibrium are typical characteristics of the DMD technique comparing conventional casting process and simulation. Grujicic et al. [15] proposed a modified CA-based method to investigate the evolution of solidification grain microstructure during the LENS rapid fabrication process. This research established the relationship between the process parameters (e.g., laser power, laser velocity) and solidification microstructure in binary metallic alloy. The finite difference analysis was also coupled with the modified CA to calculate the temperature field as the input of microstructure prediction. Kelly and Kampe [16, 17] developed the thermal history in DMD of Ti6Al4V and microstructural characterization. Nie et al. [18] developed a multiscale model to simulate microstructure evolution during laser additive manufacturing solidification. The study presented the relationship between the solidification conditions and the resultant microstructure, especially Laves phase particles in Ni-based superalloy. Rodgers et al. [19] proposed a 2D mesoscale model to simulate grain structure near a moving heat source with kinetic Monte Carlo simulator during electric beam melting (EBM) process. The method is capable of simulating both singlepass and multipass welds grain morphology. It also investigates the influence of initial substrate grain size on HAZ and FZ grain shape and size. Rai et al. [20] coupled a lattice Boltzmann (LB) and cellular automaton (CA) to simulate the microstructure evolution during electron beam melting. Initial grain selection at the base plate, grain boundary perturbation, grain nucleation due to unmolten powder particles in the bulk, grain penetration can all be simulated. The influence of process parameters on the final grain structure and texture evolution is analyzed. Keller et al. [21] investigated aspects of microstructure and microsegregation during rapid solidification in a laser powder bed fusion additive manufacturing process. Finite element analysis is employed to simulate the laser melt pool and temperature field. Microsegregation between dendritic arms is calculated by using the Scheil-Gulliver solidification model and DICTRA software. Phase field is developed to produce microstructures with primary cellular/dendritic arm spacing. However, there are few investigations on microstructure evolution prediction based on substrate and fusion zone during DMD process. Compared to other powder bed additive manufacturing process, there is different thermal cycle and the cooling rates for DMD process, which results in different microstructure. This part-level simulation on microstructure is critical because it provides the foundation for the prediction and control of mechanical properties.

CA simulation is appropriate for mesoscale modeling of grain structure because it does not consider much details inside a specific grain such as secondary dendritic arm spacing (SDAS) and microsegregation. Since it belongs to mesoscale model and does not cost as much computational resources as other microscale models, such as phase field and molecular dynamic, these characteristics of CA model make it appropriate for simulating the part-level grain structure instead of a very small region including less than a hundred grains. Thus, it can be used to predict and control the mechanical properties of the whole part based on the part-level grain structure under different parameters. Molecular dynamic (MD) simulation of microstructural evolution during additive manufacturing [22] is focused on a microscalability, which is between nanometer and micrometer. MD simulation can provide a method to investigate the crystallization process within the HAZ and clarify its crystallization mechanism because it is difficult to observe directly the crystallization process in the HAZ during the cyclic heating and cooling process. Even though MD can investigate microstructure evolution on a molecular level, it will cost too much resource to simulate the whole part structure and properties. PF model [21, 23], a microscopic one, can be used to simulate the solute concentration and phase transformation by solving the potential equation. The coefficients in the evolution equation

of phase-field variables are related to the material parameters so that it can quantitatively simulate grain growth within a finer scale compared to CA and MC. Lattice Boltzmann (LB) method is adopted to numerically simulate the solute transport within the melt pool domain because it is appropriate for the complex geometry shape and is built from the temporal and spatial discretized grid, avoiding solving macroscopic N-S equations. The computational domain is discretized into regular lattices with the same cell size as the CA model. The governing equation and boundary conditions for transport process are described in detail in Refs. [24–27]. The comparison of AM microstructure simulation methods is shown in **Table 1**. The current CAFÉ model can be used to consider multiple components if it considers the solute concentration and there is no chemical reaction and intermetallic phase formation during the solidification process. However, it is not capable of determining the mechanical properties directly if it is not incorporated with other models such as Hall-Petch model.

Methods	Advantages	Limitations
Cellular automaton	• Coupled prediction of thermal history and grain structure • Predicts microstructure with multiple heat source passes • Including crystallographic orientation and texture • Relatively low computational cost	• No HAZ grain evolution • Unavailable open source code • Lack of grain substructure
Monte Carlo	• Predicts 3D microstructures with hundreds of heat source passes • Microstructure evolution within fusion zone and HAZ • Included in the open source code	• Idealized molten zone • No direct coupling of thermal and microstructural models • Does not incorporate material texture or anisotropy.
Phase field	• Available subgrain features • Including solute concentration and phase transformation • Material parameters related to phase-field variables	• High computational cost • Small computational domain • Solving complex potential equations
Lattice Boltzmann	• Allows for coupled thermos-fluid and micro-structure evolution on same lattice • Including crystallographic orientation and texture • Appropriate for the complex geometry shape • No need to solve macroscopic N-S equations	• Unstable solutions for many regimes • No solid-state grain evolution after solidification • Unavailable open source code
Molecular dynamics	• Explain crystallization mechanism • Simulating microstructure within HAZ	• Costs too much computational resource • Very small computational region
Empirical microstructure models	• Estimates microstructural features over large parts • Allows extension of preexisting thermal models.	• Does not provide microstructure for further analysis. • Requires estimation of thermal condition.

Table 1. Comparison of AM microstructure simulation methods.

http://dx.doi.org/10.5772/intechopen.73107

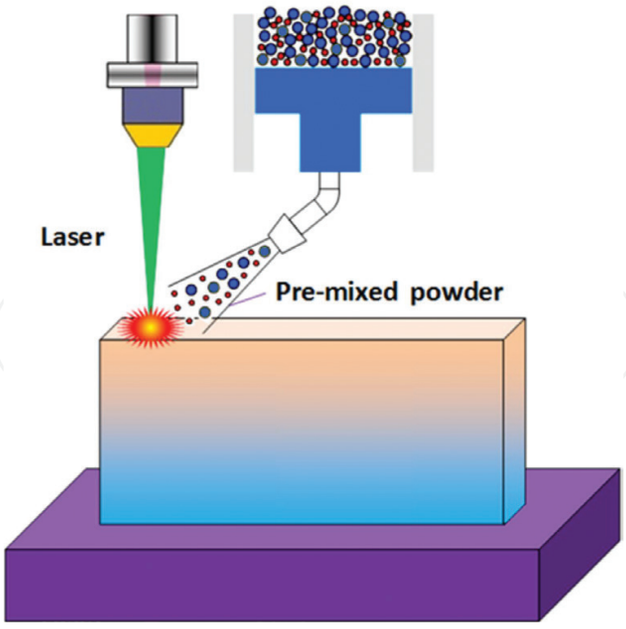

Figure 1. Laser powder deposition schematic.

In this study, a predictive multiscale model based on a cellular automaton (CA)-finite element (FE) method has been developed to simulate thermal history and microstructure evolution during metal solidification for a laser-based additive manufacturing process shown in **Figure 1**. ABAQUS was used to calculate the temperature field of the whole part, which offers the macroscopic FE nodes' temperature. In order to integrate the different scales, a coupled model is developed to combine with thermal history and simulate nucleation site, grain growth orientation and rate, epitaxial growth of new grains, remelting of preexisting grains, metal addition and grain competitive growth. Interpolation was utilized to obtain the finer nodes' temperature based on the FE nodes result. The temperature field was validated by the type K thermocouples. The CA model, which was able to show the entrapment of neighboring cells and the relationship between undercooling and the grain growth rate, was built to simulate the microstructure information such as the grain size and columnar grain orientation. The developed "decentered polygon" algorithm is more appropriate for grain structure development in the highly nonuniform temperature field. This simulation will lead to new knowledge that simulates the grain structure development of single- and multiple-layer deposition during DMD process. The microstructure simulation results were validated by the experiment. The model parameters for the simulations were based on Ti-6Al-4V material (**Figure 1**).

2. Mathematical model

2.1. Ti6Al4V transient temperature field during the deposition process

In the direct metal deposition (DMD) process, the temperature history of the whole domain directly influences the deposition microstructure, which is critical to mechanical properties [28]. In order to obtain the microstructure information during the solidification process, the temperature field must be known at each time step. The transient temperature field throughout

the domain was obtained by solving the 3D heat conduction Eq. (1), in the substrate, along with the appropriate initial and boundary conditions [29].

$$\rho(T)\cdot c_p(T)\cdot\frac{\partial T}{\partial t} = \frac{\partial}{\partial x}\left(k(T)\frac{\partial T}{\partial x}\right)+\frac{\partial}{\partial y}\left(k(T)\frac{\partial T}{\partial y}\right)+\frac{\partial}{\partial z}\left(k(T)\frac{\partial T}{\partial z}\right)+\dot{Q}, \tag{1}$$

where T is the temperature, $\rho(T)$ is the density, $c_p(T)$ is the specific heat, $k(T)$ is the heat conductivity and Q is the internal heat generation following certain energy distribution per unit volume.

The initial conditions applied to solve Eq. (1) were:

$$T(x, y, z, 0) = T_0 \text{ and } T(x, y, z, \infty) = T_0, \tag{2}$$

where T_0 is the ambient temperature. In this study, T_0 was set as room temperature, 298 K. The boundary conditions, including thermal convection and radiation, are described by Newton's law of cooling and the Stefan-Boltzmann law, respectively. The laser heating source term, $\dot{Q}$ in Eq. (1), was also considered in the boundary conditions as a surface heat source. The boundary conditions then could be expressed as [29]

$$K(\Delta T\cdot n)\big|_\Gamma = \begin{cases} \left[-h(T-T_0)-\varepsilon(T)\sigma(T^4-T_0^4)\right]\big|_\Gamma & \Gamma \notin \Lambda \\ \left[Q-h(T-T_0)-\varepsilon(T)\sigma(T^4-T_0^4)\right]\big|_\Gamma & \Gamma \in \Lambda' \end{cases} \tag{3}$$

where k, T, T_0 and Q bear their previous definitions, n is the normal vector of the surface, h is the heat convection coefficient, $\varepsilon(T)$ is the emissivity, σ is the Stefan-Boltzmann constant, which is 5.6704×10^{-8} W/m^{2}K^4, Γ represents the surfaces of the work piece and Λ denotes the surface area irradiated by the Gaussian laser beam.

In order to simulate the thermal history during the direct metal deposition more efficiently and reduce the computational cost, some assumptions were taken into account. In the experiment, a Gaussian distributed laser beam was utilized to melt the substrate vertically with a nonuniform power density [30]. Thus, the transverse intensity variation is described as Eq. (4):

$$I(r, y) = \alpha\frac{P}{\pi w(y)^2/2}\exp\left(-2\frac{r^2}{w(y)^2}\right), \tag{4}$$

where α is the laser absorption coefficient, P is the power of the continuous laser and $w(y)$ is the distance from the beam axis where the optical intensity drops to $1/e^2(\approx 13.5\%)$ of the value on the beam axis. α was set as 0.4 based on numerical experiments in the LAMP laboratory and $w(y)$ is 1 mm in this simulation. The motion of laser beam was simulated by adjusting the position of beam center R with programming a user subroutine "DFLUX" in ABAQUS. The formula of R is as follows:

$$R = \left[\left(x-\int_{t_0}^{t} u dt\right)+\left(y-\int_{t_0}^{t} v dt\right)+\left(z-\int_{t_0}^{t} w dt\right)\right]^{1/2}, \tag{5}$$

where x, y and z are the spatial coordinates of the Gaussian laser beam center, and u, v and w are the laser moving velocities.

The Marangoni effect caused by the thermocapillary phenomena can directly influence the temperature field in the whole domain, so it is considered to obtain more accurate thermal history during DMD [31]. The artificial thermal conductivity was put forward to address the Marangoni effect in the finite element method [32]

$$k_m(T) = \begin{cases} k(T), & T \le T_{liq} \\ 2.5k(T), & T > T_{liq} \end{cases}, \tag{6}$$

where k_m is the modified thermal conductivity and T_{liq} is the liquidus temperature.

In the FEA model, the powder addition was simulated by activating elements in many small steps [33]. The width of the deposit area is assumed to be the same as the Gaussian laser beam. The thickness of each layer is calculated by transverse speed, powder feed rate and powder absorption efficiency. The deposit geometry, boundary condition and heat flux were updated after each step.

2.2. Ti6Al4V morphology prediction after solidification

Heterogeneous nucleation occurs nearly instantaneously at a characteristic undercooling. The locations and crystallographic orientation of the new nuclei are randomly chosen at the surface or in the liquid. As explained by Oldfield [34], the continuous nucleation distribution, $dn/d\Delta T'$, which characterizes the relationship between undercooling and the grain density, is described by a Gaussian distribution both at the mold wall and in the bulk liquid. The parameters of these two distributions, including maximum nucleation density n_{max}, the mean undercooling ΔT_N and the standard deviation of the grain density distribution ΔT_σ, can be obtained from experiments and grain size measurements. The grain density, $n(\Delta T)$, is given by Eq. (7):

$$n(\Delta T) = \int_0^{\Delta T} \frac{dn}{d\Delta T'} d\Delta T' = \int_0^{\Delta T} \frac{n_{max}}{\Delta T_\sigma \sqrt{2\pi}} exp\left[-\frac{1}{2}\left(\frac{\Delta T' - \Delta T_N}{\Delta T_\sigma}\right)\right] d\Delta T', \tag{7}$$

where n_{max} is the maximum nucleation density of nucleation grains, which is obtained by the integral of the nucleation distribution (from zero undercooling to infinite undercooling). ΔT_N and ΔT_σ are the mean undercooling and standard deviation of the grain density distribution, respectively. Here, all temperatures are in Kelvin.

Undercooling is the most important factor in the columnar and dendrite growth rate and grain size. The total undercooling of the dendritic tip consists of three parts such as solute undercooling, thermal undercooling and curvature undercooling. For most metallic alloys, the kinetic undercooling for atom attachment is small, so it is neglected [35]. The total undercooling can be calculated as follows:

$$\Delta T = m C_0\left[1 - A(P_C)\right] + \theta_t I(P_t) + \frac{2\Gamma}{R}, \tag{8}$$

where m is the liquidus slope, Γ is the Gibbs-Thomson coefficient, C_0 is the solute concentration in the liquid far from the solid-liquid interface, P_t and P_c are the thermal and solutal Peclet numbers, respectively, k is the solute partition coefficient at the solid-liquid interface, $A(P_c)$ equals $[1-(1-k)I(P_c)]^{-1}$, θ_t is the unit thermal undercooling $(=\Delta h_f/c)$ and R is the radius of the dendritic tip.

For the laser deposition process, the rapid solidification condition corresponds to a high Peclet number at which the dendritic tip radius is given by Eq. (9)

$$R = \left[\frac{\Gamma}{\sigma^*(m G_c^* - G^*)}\right]^{1/2}, \tag{9}$$

where σ^* is the marginal stability constant, approximately equals $1/4\pi^2$ [36], and G^* and G_c^* are the effective temperature gradient and concentration gradient, respectively.

2.3. Coupling macroscopic FE and mesoscopic CA models

The temperature field result can be used to calculate enthalpy increment, which is necessary to calculate enthalpy at each time step. A linearized implicit FE enthalpy formulation of the heat flow equation can be given [10]

$$\left[\frac{1}{\Delta t}\cdot[M] + [K]^t\left[\frac{\partial T}{\partial H}\right]^t\right]\cdot\{\delta H\} = -\{K\}^t\cdot\{T\}^t + \{b\}^t, \tag{10}$$

where {M} is the mass matrix, {K} is the conductivity matrix, {b} is the boundary condition vector and {T} and {H} are the temperature and enthalpy vectors at each node of the FE mesh, respectively. The Newton method and Euler implicit iteration are included in (10). This set of equations can be solved using the Gauss elimination method for {δH}.

$$\delta H = \rho\cdot c_p\cdot[T^{t+\delta t} - T^t] - \Delta H_f\cdot\delta f_s. \tag{11}$$

Thus, the next time-step enthalpy can be obtained by the relationship of $H_i^{t+1} = H_i^t + \delta H$. The new temperature field can be obtained from the coupling model using (11). ΔH_f is the latent heat of fusion per unit volume. f_s represents the fraction of solid. δf_s can be calculated as in [10].

In the FE macroscopic model, the temperature field was calculated on a relatively coarse mesh, but the solidification microstructure had to be developed on a finer regular CA mesh with a cell size in the order of the secondary dendrite arm spacing (SDAS). **Figure 2** indicates the interpolate relationship between coarse FE nodes and fine CA cells. The known temperature T_n^t and the volumetric enthalpy variation δH_n were interpolated into the CA network by the linear interpolation in Eqs. (12) and (13). ϕ_{vn} is the interpolation coefficient. Every CA cell temperature in the calculation domain can be obtained with this interpolation.

$$T_v^t = \sum_n \phi_{vn}\cdot T_n^t \tag{12}$$

$$H_v^t = \sum_n \phi_{vn}\cdot H_n^t \tag{13}$$

http://dx.doi.org/10.5772/intechopen.73107

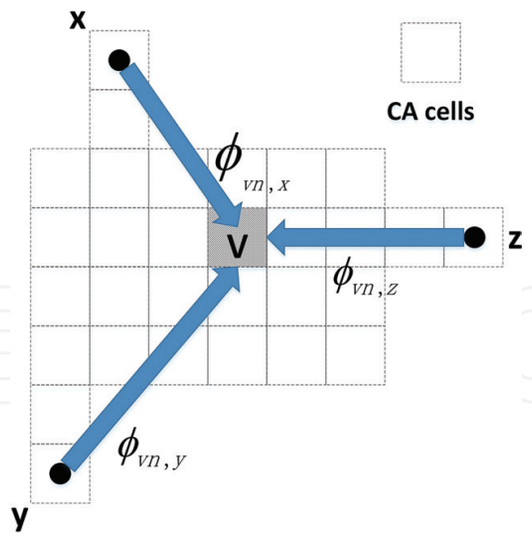

Figure 2. x, y and z represent the FE temperature nodes (coarse grids) and v represents the CA cells (fine grids). The three linear interpolation coefficients from FE nodes x, y and z to CA cells v are ϕ vn,x, $\phi_{vn,y}$ and $\phi_{vn,z}$.

The finer temperature, T_v^t, and enthalpy variations, δH_v^t, in regular CA cells were used in Eq. (13) to yield the temperature in the next microtime step. After a few microtime steps, the temperature field in the CA network could be substituted into the coarser nodes of the macroscopic model. The interpolated temperature field is employed as the model input. Heterogeneous nucleation, grain growth orientation and grain growth are solved in the CA-FE model in

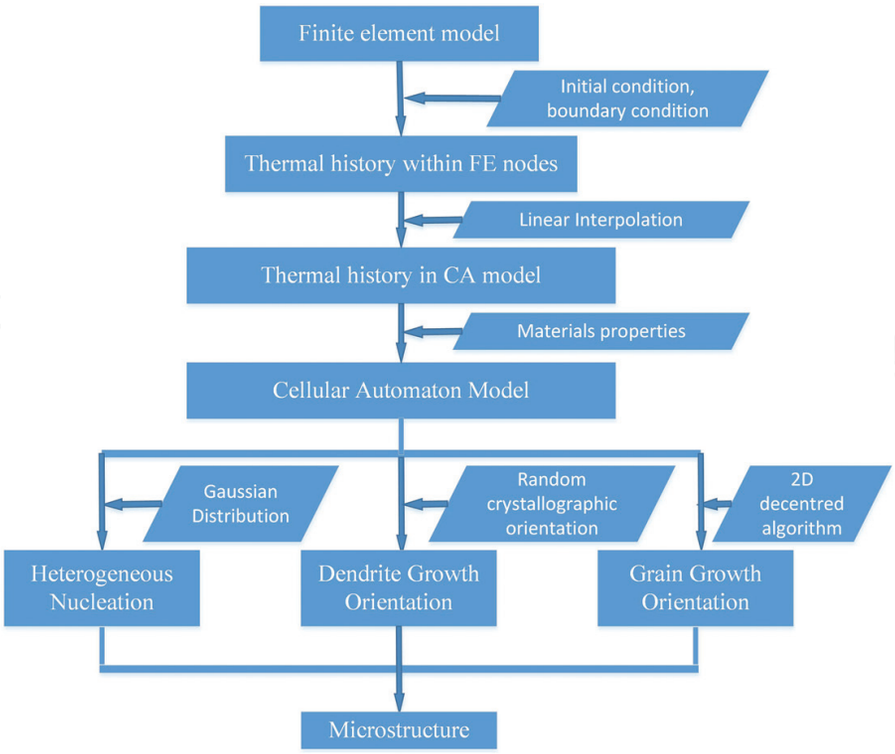

Figure 3. Flow chart of the coupling CA-FE model.

terms of nucleation location distribution, random crystallographic orientation and CA cells capture. **Figure 3** indicates the flow chart of coupling FE-CA model. The details of the CA growth algorithm are shown in **Figure 4**.

Figure 5 illustrates the conventional and modified cell capture algorithm. For the conventional method, the vertices of the square envelope move along the diagonal, and the growth of the square envelope is determined by the center cell temperature, not local temperature, at each time step, which results in the same growth rate for the four vertices. The grain orientation will be along with the axis of computational domain after a few time steps, thus, losing its original orientation information. The modified "decentered polygon" algorithm is implemented to control the grain growth within the melt pool and at the sold/liquid interface. Compared to the traditional "decentered square" algorithm of cell capturing, the modified "decentered polygon" algorithm does not need to create square for each cell when it begins to grow. Only the decentered polygon of a starting nucleated cell is tracked during the grain growth process, which reduces the computational cost. Besides, the modified algorithm can prevent grain orientations from realigning with x axis after a few growing steps because each cell will stop growing when Von Neumann and Moore neighbors are both solid. The controlling point growth rate is determined by the local cell temperature. Therefore, the region with higher thermal gradient will solidify faster along the steepest thermal gradient.

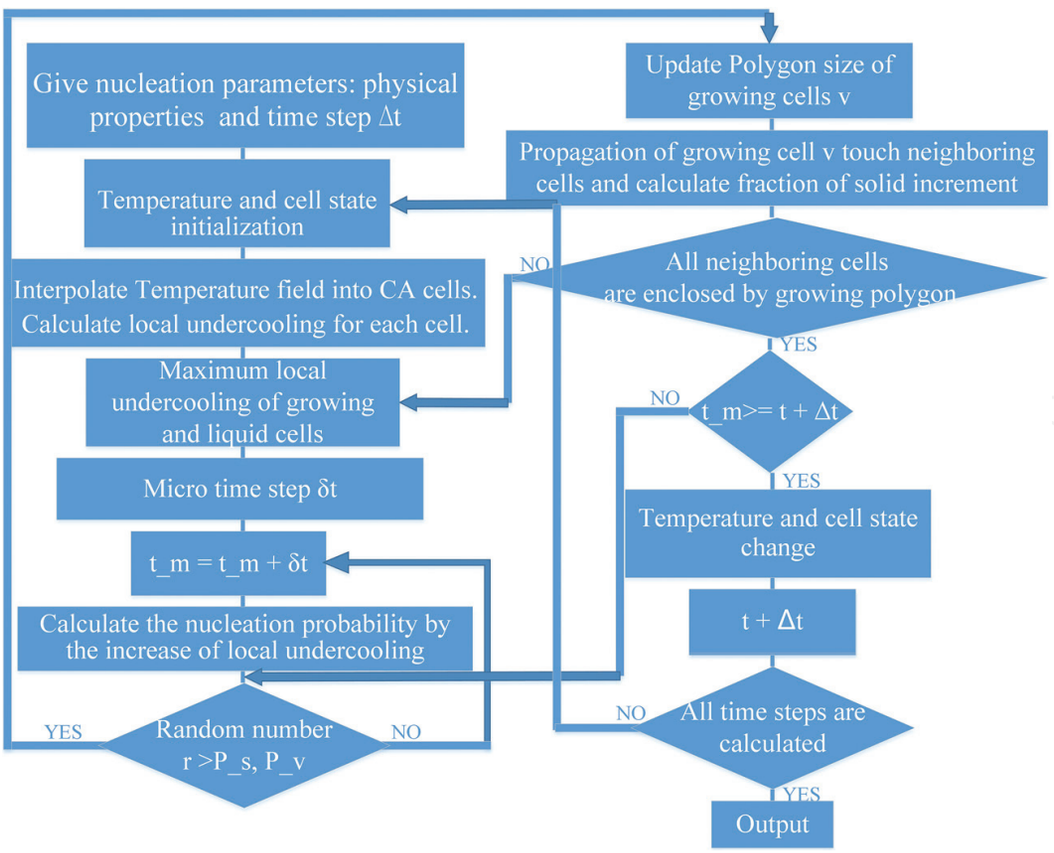

Figure 4. Flow chart of CA algorithm.

http://dx.doi.org/10.5772/intechopen.73107

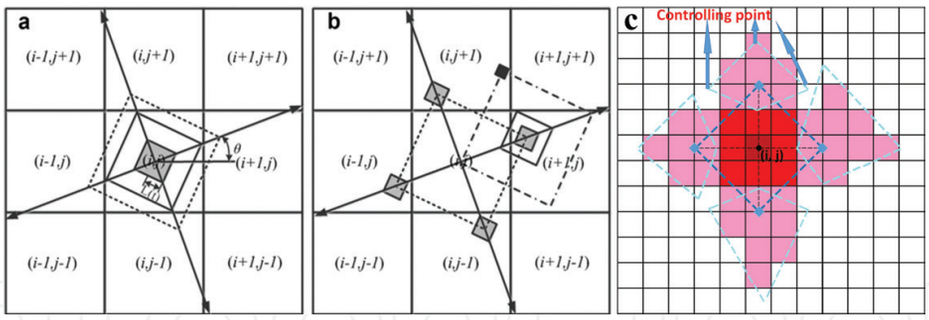

Figure 5. Illustration of the conventional and modified cell capture algorithm: (a) capturing rule of cell (i, j) within a decentered square, (b) capturing rule of eight neighboring cells before (i, j) growth termination [37] and (c) the modified cell capture and growth algorithm of "decentered polygon" with neighboring cells effect for cubic crystal alloys.

3. Results and discussion

3.1. Single-layer temperature and grain structure

The deposition temperature field and grain morphology were simulated first only in one layer. **Figure 6** shows thermal history of the whole block during the DMD process. **Figure 6(a)** indicates the temperature field of the whole block when laser beam is passing along the x direction at time = 1.0 s, while **Figure 6(b)** shows the temperature field when substrate cools down with laser off at time = 29.0 s. The total physical time of single-layer laser deposition is 2 s, while the cooling time is 28 s in the simulation. For each step, the step time is 0.1 s when the laser is shot on the surface of the deposited material. After 30 s of cooling down, the temperature distribution is more uniform. **Figure 7** indicates the thermal history of two nodes, which locate at the center point in the deposit and 1 mm away from the deposit. The result shows that the highest temperature in the deposit is approximately 2884 K, which occurred at the center of the Gaussian beam. The center node at 1 mm away from the deposit arrives at peak temperature of 1126 K that cannot melt the Ti6Al4V substrate. Based on every node's thermal history, the undercooling (discrepancy between liquidus temperature and current temperature) that is critical to resulting in grain nucleation and growth rate can be determined.

In order that the input of microstructure model is reliable, the temperature field is validated with four type-K thermocouples. The locations are shown in **Figure 8**. One is located at the starting of laser path, which distance to the laser is approximately 3–3.5 mm. Another three points are located by one side of laser path, which distance to the laser center is approximately 2 mm. Arduino device is used to sample the temperature data. A laser deposition experiment is conducted with the power of 750 W, scanning speed of 600 mm/min and 2 g/min for single-layer deposit. The difference between the experiment and the FEM modeling is less than 10°C shown in **Figure 9**. In **Figure 9(a)**, the delay between the simulated temperature and the thermocouple itself is more visible than **Figure 9(b)–(d)** because the distance of first thermocouple point is further than other three ones. In the real experiment, the substrate is fixed by the metal fixture, which resulting in the more heat conduction than the FEM model. Because of argon gas, forced convection occurred in the real experiment. This also causes lower cooling

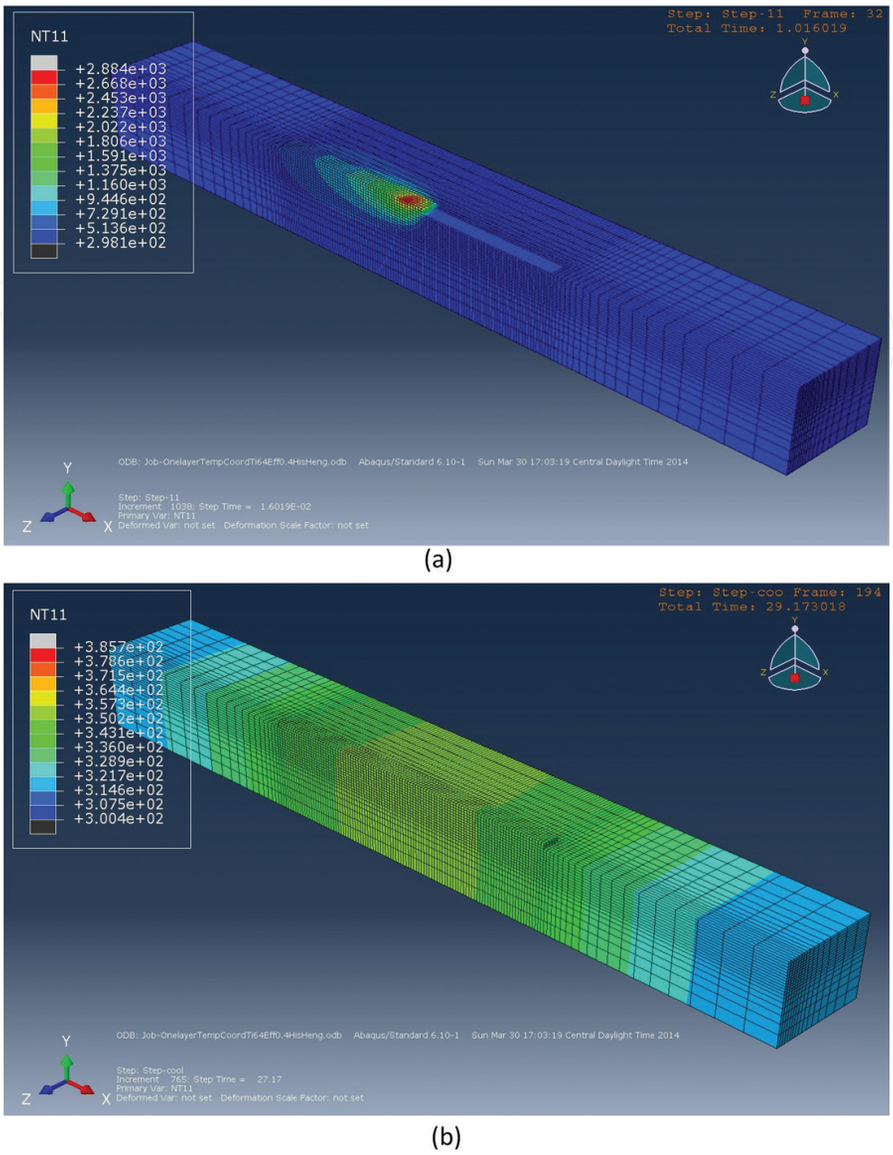

Figure 6. Cross-sectional simulated temperature distribution during single-layer laser deposition process. The deposition time is 2 s, while the cooling time is 28 s. (a) Temperature field at time = 1.0 s and (b) temperature field at time = 29.0 s.

rate in the temperature simulation. Because the difference between experiment and simulation is smaller than 10%, the current FEA modeling is still considered as a reasonable simulation of temperature field, which can provide the reliable thermal input for the CA model.

A laser deposition experiment is conducted with the power of 700 W, scanning speed of 600 mm/min and 2 g/min for single-layer deposit. For this case, the cross section shown in the figure is the computational domain. The cell size for this simulation is 6 × 6 μm. X and Y axes represent the number of cells. The simulation result from conventional method is shown in **Figure 10**. It can be observed that even though different grains own diverse orientation at the very beginning, the crystallographic orientation preference tends to be along with the axis after several time steps. Here, different colors represent various grain orientations. Finally, the equiaxed grains dominate the fusion zone. The original grain orientations are not kept during the solidification process. It does not agree well with the single-layer experimental result shown in **Figure 12**.

http://dx.doi.org/10.5772/intechopen.73107

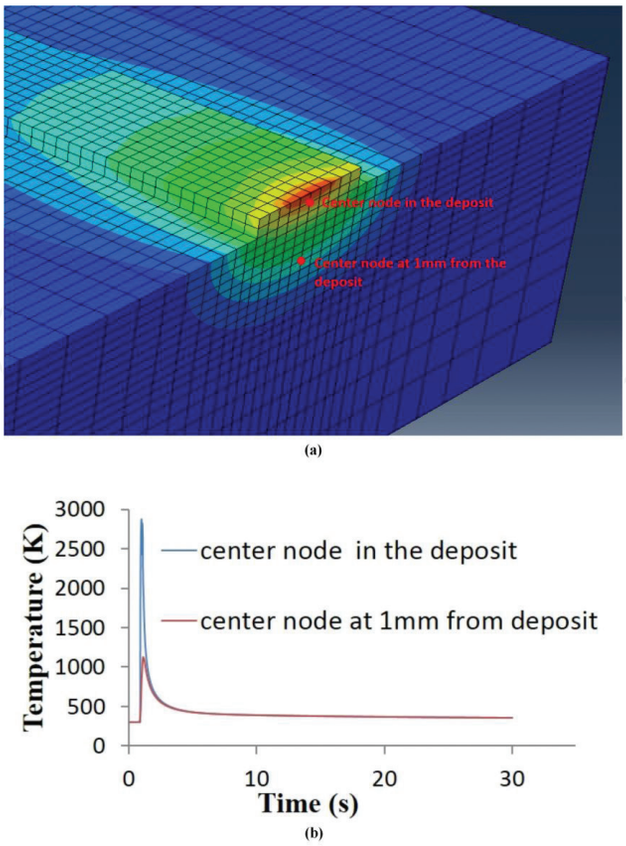

Figure 7. (a)Temperature field at t = 1s (b) Temperature history at the center node in the deposit and substrate.

The developed CA grain growth method is implemented under the same condition. According to the developed CAFÉ simulation, the single layer simulation result is shown in **Figure 11**. The grain keeps its original crystallization orientation when grain growth is modeled. The columnar grain can be identified from the solid/liquid interface. When grains continue to grow toward melt pool center, some grains overgrow other grains such that there are fewer grains further away from the solid/liquid interface.

Three samples of single-layer deposits are prepared with EDM cutting, grinding, polishing and etching. The optical microscope is shown in **Figure 12**. The comparison between simulation and experimental results is shown in **Figure 13**. An average of 20 measurements per sample is performed to determine the average grain size. It compares the experimental aver-

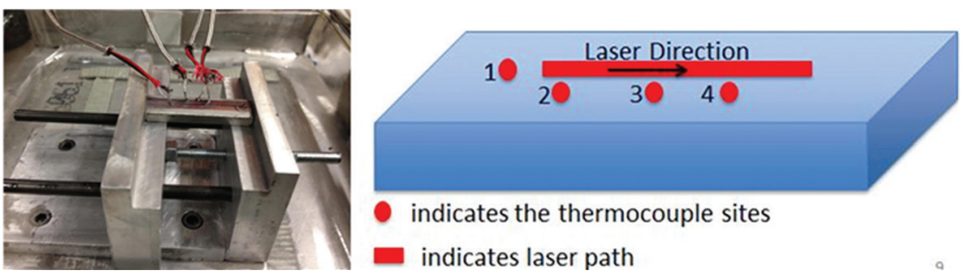

Figure 8. Thermocouples location and laser scan direction schematic diagram.

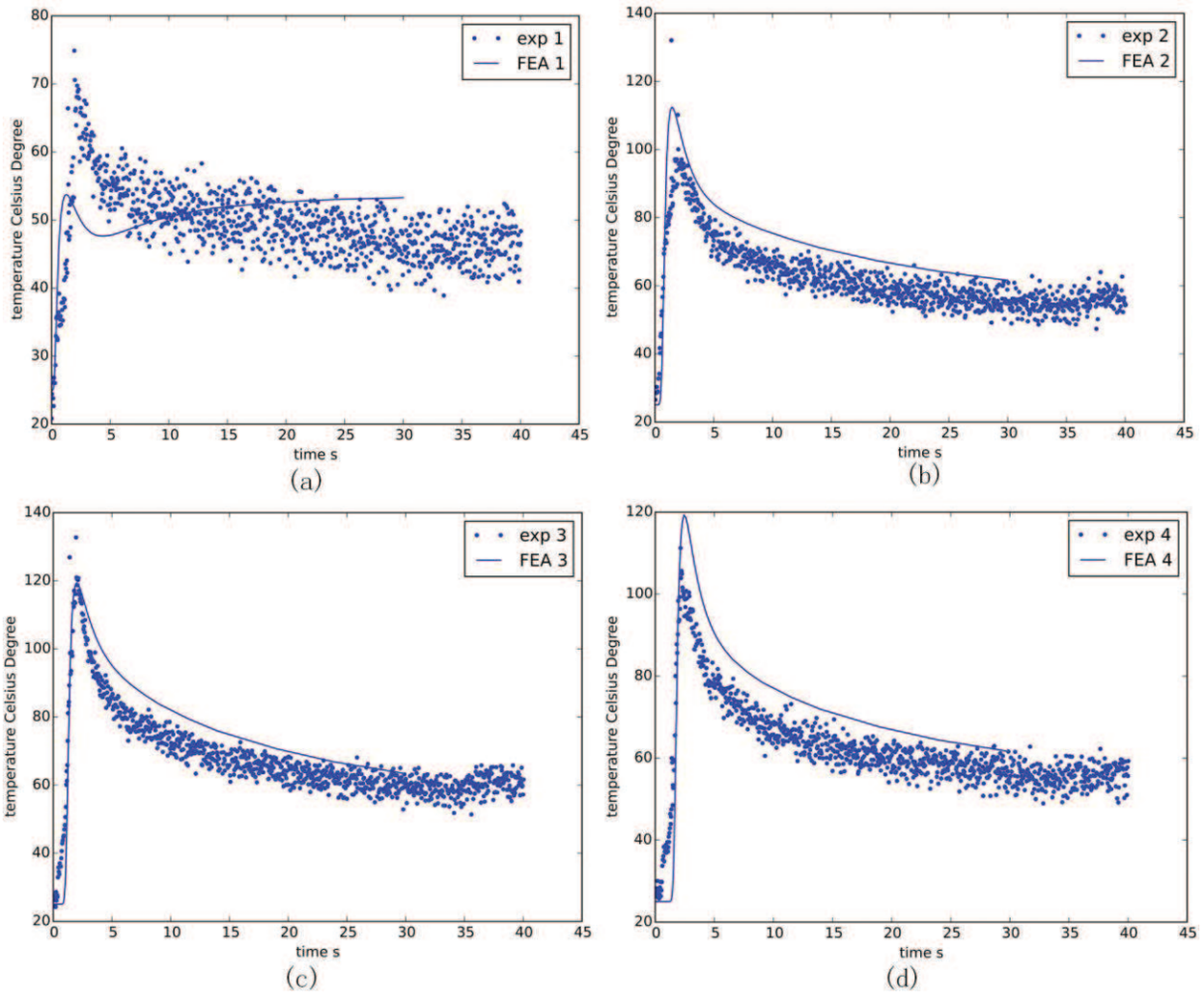

Figure 9. Temperature validation with four type-K thermocouples. (a), (b), (c) and (d) are measured at location 1, 2, 3 and 4, respectively.

age grain size with the predicted one. The shown data suggest that a 15% error between experimental measurements and predictions is present. This can be considered as a reasonable prediction of grain morphology and size.

3.2. Multilayer temperature and grain structure

Figure 14 depicts the temperature field of the substrate and deposited material, including the 25-layer deposition materials added on the substrate when the laser is moved forward and backward. The laser deposition of multiple-layer Ti-6Al-4V was conducted with the power of 750 W, scanning speed of 200 mm/min and powder delivery of 2 g/min. The elemental size is nonuniform along the three directions because it is not necessary to apply fine elements to where the location is far from the molten pool. **Figure 15** shows that the thermal history and peak temperature of different layers are not identical. The higher layer performs higher thermal history because the higher layer accumulates more heat than the lower one, and it is closer to heat source.

http://dx.doi.org/10.5772/intechopen.73107

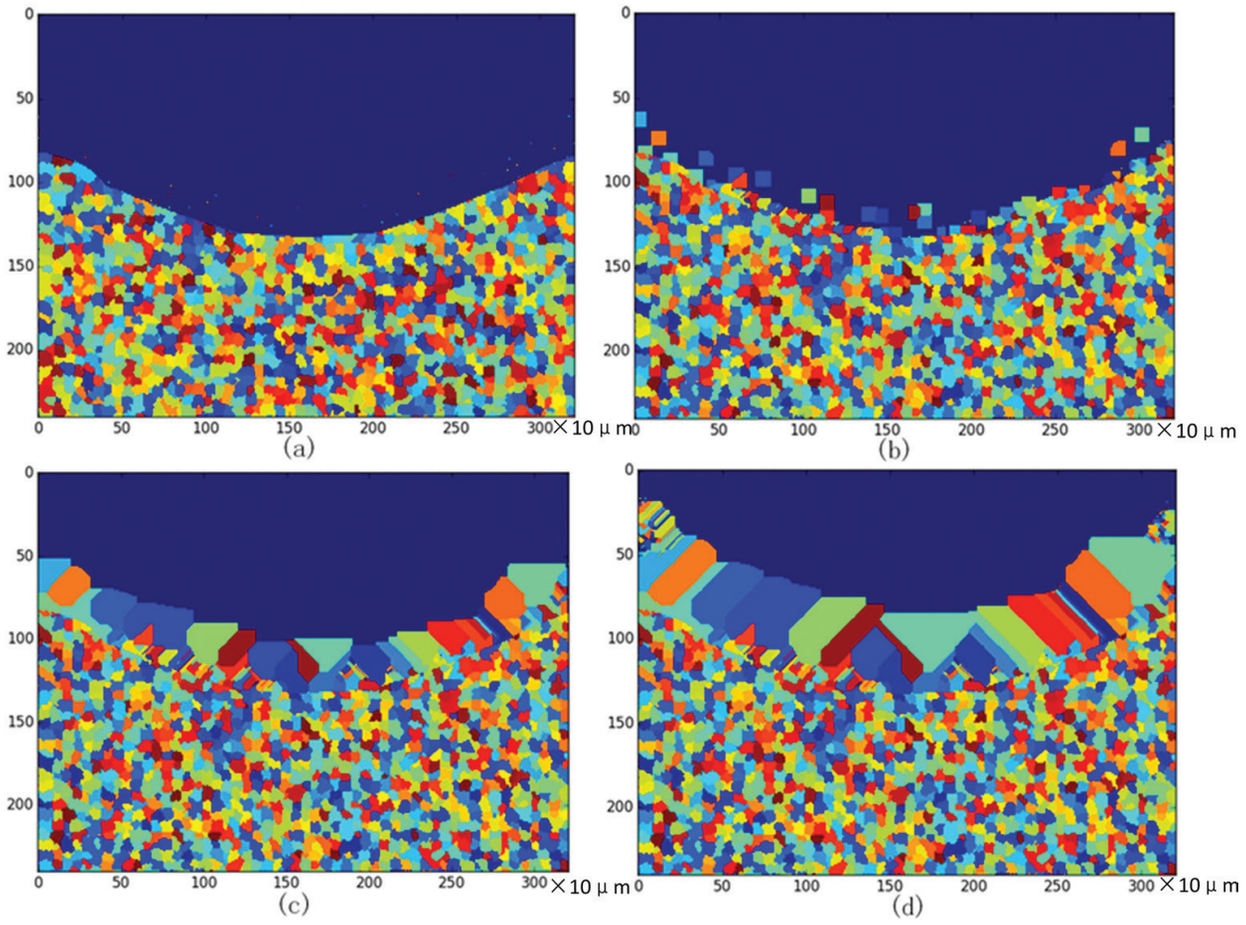

Figure 10. Grain structure of conventional growth method for single-layer Ti6Al4V deposition at (a) 5 ms, (b) 25 ms, (c) 45 ms and (d) 65 ms time step.

Figure 16 shows Ti-6Al-4V deposition grain microstructure. The cross-sectional dimension of deposit region is 1.8 × 1.9 mm, which is close to 2 × 2 mm assumption in the simulation. In **Figure 16**, it can be observed that at the bottom deposition, crystallographic orientation is not only limited to the vertical direction. It can also be observed that columnar grains dominate in the laser deposition area. **Figure 16(a)** and **(b)** indicates the whole deposition region at different magnification and the locations of top and bottom region, while **Figure 16(c)** and **(d)** shows the grain size and shape with higher magnification. Under the same condition, the experiment is conducted, and the optical microscope images are taken. **Figure 16(e)** shows multiple layers of the Ti-6Al-4V grain morphology under the laser deposition process. Irregular grain shape and size can be obtained. When more layers were deposited, prior β columnar grains began to dominate, while equiaxed grains began disappearing. As the solidification process continues, competitive growth among different grains occurs. Therefore, the size of columnar grain increases, and the number of grains goes down. The orientations of the columnar grains were almost perpendicular to the laser motion's direction because the grains grew along the steepest thermal gradient direction. This phenomenon verifies the columnar grain orientation in the simulation result. The domain size in the CA model was 2 × 2mm. After measurement of grain size, it can be found in **Figure 17** that in the simulation, the grain size ranges from 113 to 346 μm. For the

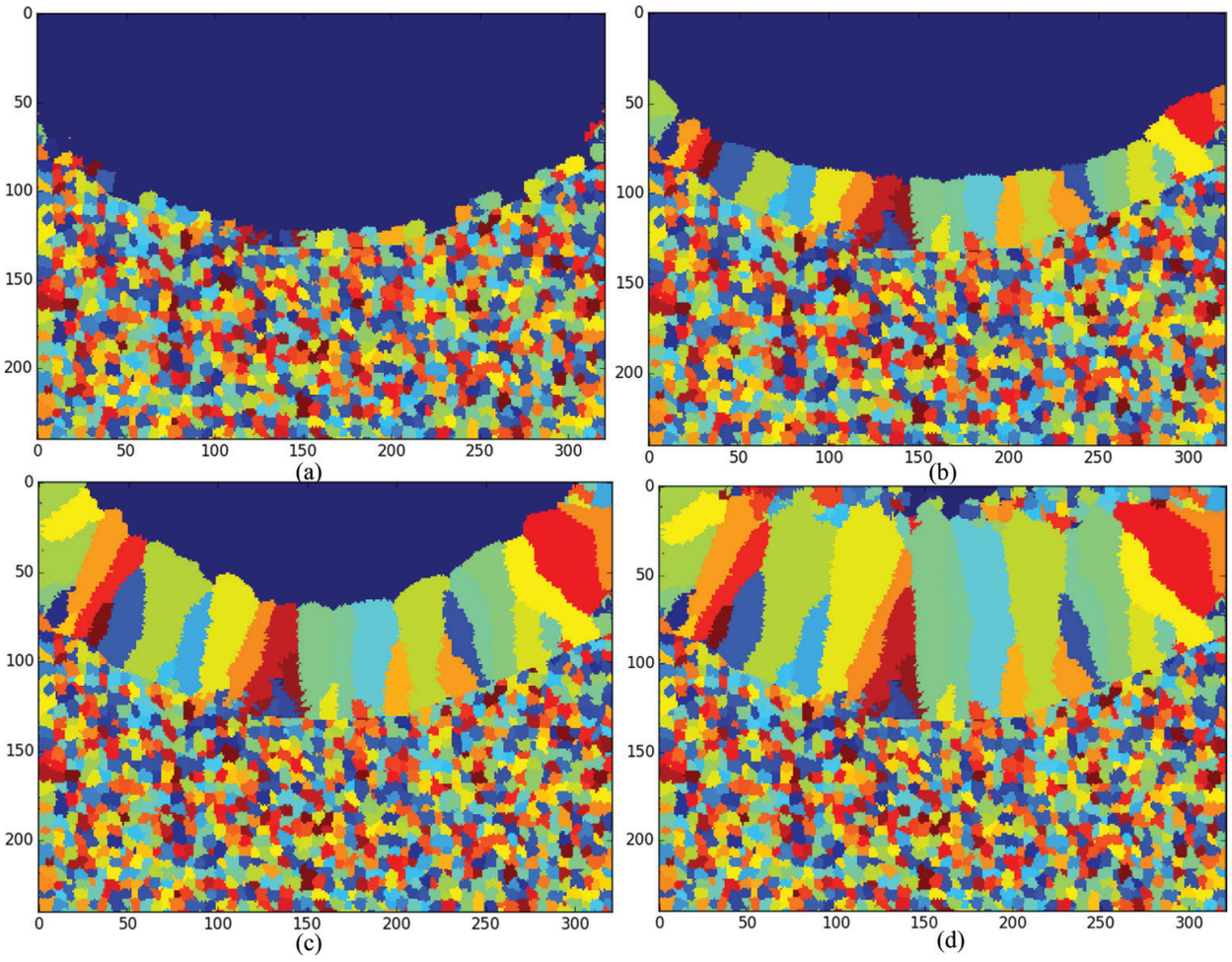

Figure 11. Grain structure of developed growth method for single-layer Ti6Al4V deposition at (a) 20 ms, (b) 40 ms, (c) 60 ms and (d) 80 ms time step.

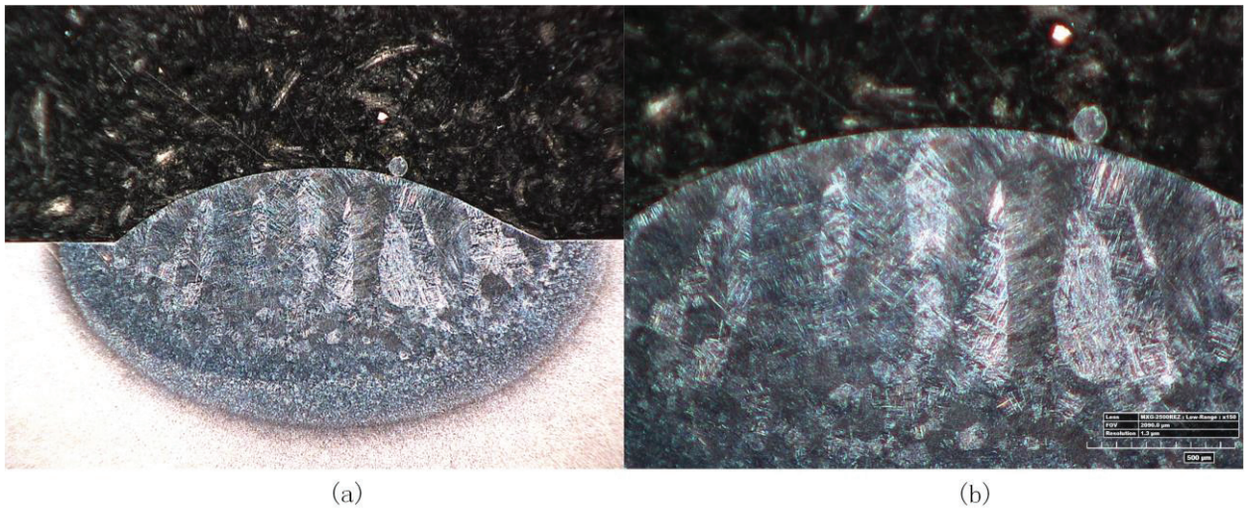

Figure 12. Ti-6Al-4V single-layer deposition grain morphology at (a) 50x and (b) 200x.

http://dx.doi.org/10.5772/intechopen.73107

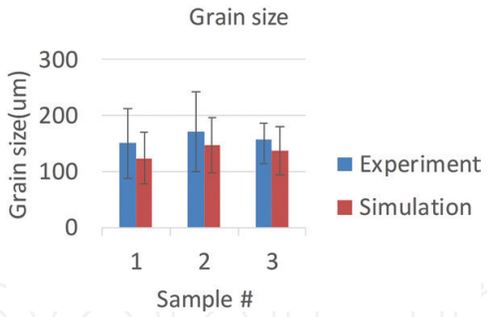

Figure 13. Grain size comparison between simulation and experiment.

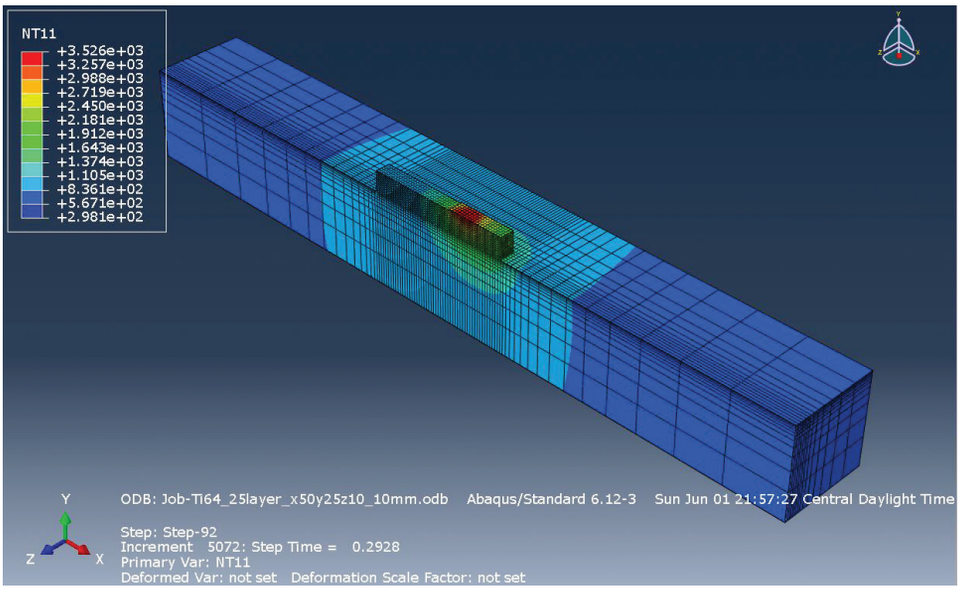

Figure 14. Thermal history for 25-layer Ti-6Al-4V laser deposition. This figure shows the 18th layer deposit temperature field.

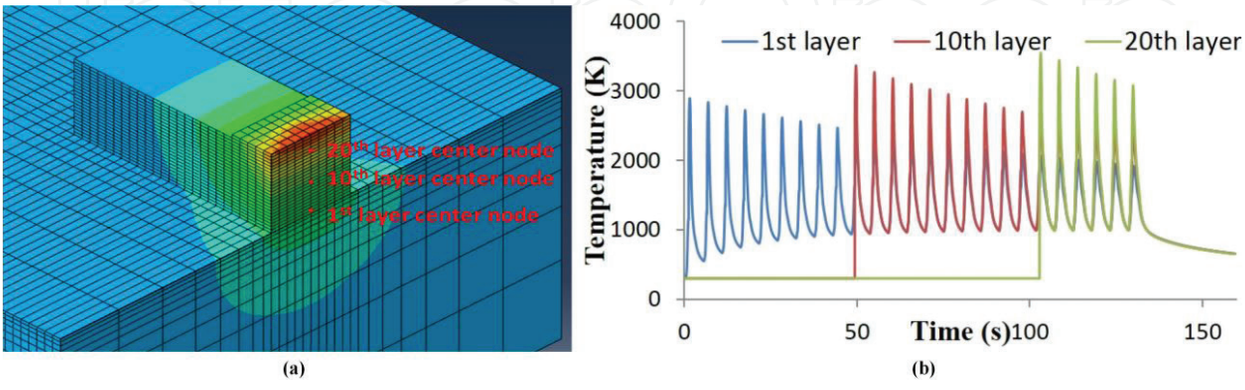

Figure 15. (a) Three nodes location cross section schematic and (b) thermal history of the center node at 1st, 10th and 20th layer.

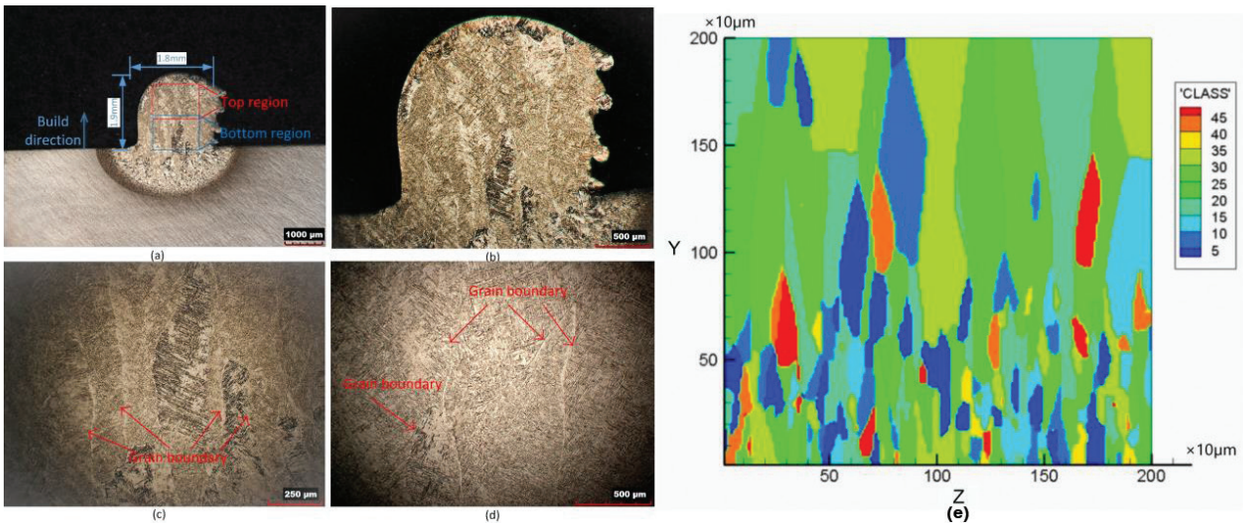

Figure 16. Ti-6Al-4V deposition grain morphologies. (a) and (b) The whole deposition, (c) the bottom region deposition and (d) the top region deposition. (e) Grain morphology modeling of 25-layer Ti-6Al-4V laser deposition. In the legend, "CLASS" represents orientations of different grains. Y and Z coordinates are in agreement with 25-layer thermal history result.

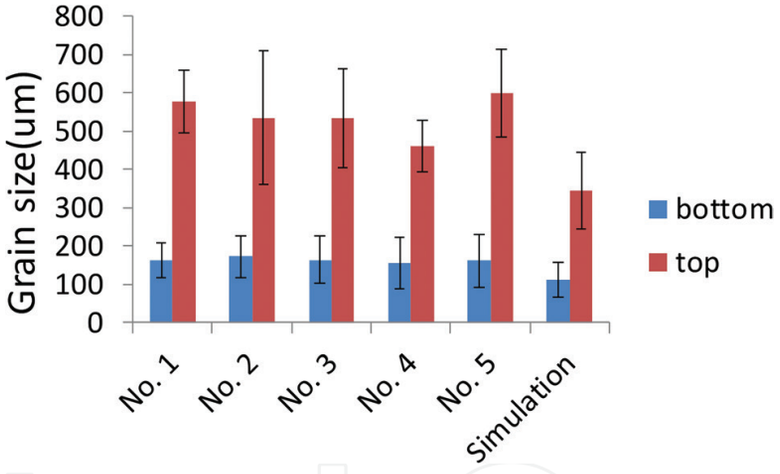

Figure 17. Grain size comparison of multiple layers between simulation and experiment.

experiment, the grain size ranges from 156 to 599 μm. The grain size at the bottom and top is larger than the simulation. This may be because it does not consider the cyclic heating and cooling process' effect on the solidified grain evolution. Usually, cyclic heating will coarsen the grain and make the grain become larger. This effect will be solved in the future research task.

Figure 18 presents the simulated grain structure from Rai et al. [20] during powder bed additive manufacturing. It can be seen that some grains overgrow others at the top layers, and most surviving grains have negative misorientations indicating grain orientation is aligned well with the beam scanning direction. The detailed local grain boundary misorientation is determined by local thermal gradient and the neighboring grains' orientation. The rate of overgrowth process also has an effect on the grain boundary angle. Compared to multiple layer results in this investigation, it shows the similarity of grain overgrowth mechanism

http://dx.doi.org/10.5772/intechopen.73107

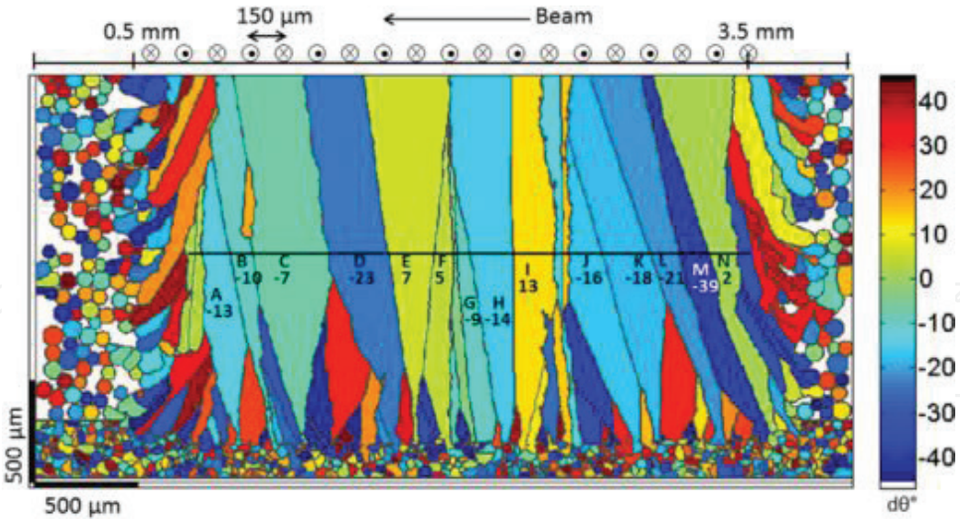

Figure 18. Simulated grain structure from Rai et al. [20]. The color bar maps grain misorientation with respect to the build direction.

and misorientation distribution. The grain size between two results is not similar because the thermal gradient and cooling rate are different between powder bed-based additive manufacturing and DMD process.

4. Conclusions

The transient temperature field of single-layer and multiple-layer deposition of Ti-6Al-4V was simulated with finite element method. The simulation result was validated by thermocouple experiment. The FE model provides the temperature at a relatively coarse scale (200 μm), and interpolation algorithm was used to scale the temperature field to match that of the CA model. The FE-CA model predicts grain morphology evolution as the deposition cools down. Hence, the instantaneous nucleation law, grain growth and crystallographic orientation were modeled in this study. It has been found that the developed "decentered polygon" growth method is more appropriate for the highly nonuniform temperature field, and the simulation result is closer to the real experimental measurement compared to the conventional growth method. For multi-layer deposit, columnar grains dominated in the 25-layer deposition in the simulation. The grain size becomes larger when the position is closer to the top area of the deposition, which matches well with the optical microscopic result. The grain size of single and multiple layers between simulation and experiment is similar. It demonstrates that this FE-CA simulation can reasonably predict thermal history and grain morphology during this case of direct metal deposition.

Acknowledgements

This work was funded through NASA's Fundamental Aeronautics Program, Fixed Wing Project, under NRA NNX11AI73A.

Author details

Jingwei Zhang*, Lei Yan, Wei Li and Frank Liou

*Address all correspondence to: jnzzp5@mst.edu

Department of Mechanical Engineering, Missouri University of Science and Technology, Rolla, MO, United States

References

[1] Rappaz M. Modelling of microstructure formation in solidification processes. International Materials Reviews. 1989;**34**(3):93-124

[2] Anderson M, Srolovitz D, Grest G, Sahni P. Computer simulation of grain growth—I. Kinetics. Acta Metallurgica. 1984;**32**(5):783-791

[3] Srolovitz DJ, Anderson MP, Sahni PS, Grest GS. Computer simulation of grain growth—II. Grain size distribution, topology, and local dynamics. Acta Metallurgica. 1984;**32**(5):793-802

[4] Saito Y, Enomoto M. Monte Carlo simulation of grain growth. ISIJ International. 1992; **32**(3):267-274

[5] Chen L-Q. Phase-field models for microstructure evolution. Annual Review of Materials Research. 2002;**32**:113-140

[6] Krill CE III, Chen L-Q. Computer simulation of 3-D grain growth using a phase-field model. Acta Materialia. 2002;**50**(12):3059-3075

[7] Böttger B, Eiken J, Steinbach I. Phase field simulation of equiaxed solidification in technical alloys. Acta Materialia. 2006;**54**(10):2697-2704

[8] Moelans N, Blanpain B, Wollants P. An introduction to phase-field modeling of microstructure evolution. Calphad. 2008;**32**(2):268-294

[9] Rappaz M, Gandin C-A. Probabilistic modelling of microstructure formation in solidification processes. Acta Metallurgica et Materialia. 1993;**41**(2):345-360

[10] Gandin C-A, Rappaz M. A coupled finite element-cellular automaton model for the prediction of dendritic grain structures in solidification processes. Acta Metallurgica et Materialia. 1994;**42**(7):2233-2246

[11] Gandin C-A, Desbiolles J-L, Rappaz M, Thevoz P. A three-dimensional cellular automation-finite element model for the prediction of solidification grain structures. Metallurgical and Materials Transactions A: Physical Metallurgy and Materials Science. 1999;**30**(12):3153-3165

[12] Choudhury A, Reuther K, Wesner E, August A, Nestler B, Rettenmayr M. Comparison of phase-field and cellular automaton models for dendritic solidification in Al–Cu alloy. Computational Materials Science. 2012;**55**:263-268

[13] Dore X. Modelling of microsegregation in ternary alloys: Application to the solidification of Al–Mg–Si. Acta Materialia. 2000;**48**:3951-3962

[14] Jarvis DJ, Brown SGR, Spittle JA. Modelling of non-equilibrium solidification in ternary alloys: Comparison of 1D, 2D, and 3D cellular automaton finite difference simulations. Materials Science and Technology. 2000;**16**(December):2-6

[15] Grujicic M, Cao G, Figliola RS. Computer simulations of the evolution of solidification microstructure in the LENS TM rapid fabrication process. Applied Surface Science. 2001;**183**:43-57

[16] Kelly SM, Kampe SL. Microstructural evolution in laser-deposited multilayer Ti-6Al-4V builds: Part II. Thermal modeling. Metallurgical and Materials Transactions A: Physical Metallurgy and Materials Science. 2004;**35**(6):1869-1879

[17] Kelly SM, Kampe SL. Microstructural evolution in laser-deposited multilayer Ti-6Al-4V builds: Part I. Microstructural characterization. Metallurgical and Materials Transactions A: Physical Metallurgy and Materials Science. 2004;**35**(6):1861-1867

[18] Nie P, Ojo OA, Li Z. Numerical modeling of microstructure evolution during laser additive manufacturing of a nickel-based superalloy. Acta Materialia. 2014;**77**(Supplement C): 85-95

[19] Rodgers TM, Madison JD, Tikare V, Maguire MC. Predicting mesoscale microstructural evolution in electron beam welding. JOM. 2016;**68**(5):1419-1426

[20] Rai A, Helmer H, Körner C. Simulation of grain structure evolution during powder bed based additive manufacturing. Additive Manufacturing. 2017;**13**(Supplement C):124-134

[21] Keller T, Lindwall G, Ghosh S, Ma L, Lane BM, Zhang F, Kattner UR, Lass EA, Heigel JC, Idell Y, Williams ME, Allen AJ, Guyer JE, Levine LE. Application of finite element, phase-field, and CALPHAD-based methods to additive manufacturing of Ni-based superalloys. Acta Materialia. 2017;**139**(Supplement C):244-253

[22] Guo S, Wang M, Zhao Z, Zhang YY, Lin X, Huang WD. Molecular dynamics simulation on the micro-structural evolution in heat-affected zone during the preparation of bulk metallic glasses with selective laser melting. Journal of Alloys and Compounds. 2017;**697**:443-449

[23] Militzer M. Phase field modeling of microstructure evolution in steels. Current Opinion in Solid State & Materials Science. 2011;**15**(3):106-115

[24] Wolf-Gladrow DA. Lattice-Gas Cellular Automata and Lattice Boltzmann Models. Springer Berlin Heidelberg; 2000

[25] Zhou JG. A lattice Boltzmann method for solute transport. International Journal for Numerical Methods in Fluids. 2009;**61**(8):848-863

[26] Rai A, Markl M, Körner C. A coupled Cellular Automaton–Lattice Boltzmann model for grain structure simulation during additive manufacturing. Computational Materials Science. 2016;**124**:37-48

[27] Yin H, Felicelli SD, Wang L. Simulation of a dendritic microstructure with the lattice Boltzmann and cellular automaton methods. Acta Materialia. 2011;**59**(8):3124-3136

[28] Lütjering G. Influence of processing on microstructure and mechanical properties of (α+β) titanium alloys. Materials Science and Engineering A. 1998;**243**(1-2):32-45

[29] Reddy JN, Gartling DK. The Finite Element Method in Heat Transfer and Fluid Dynamics. New York: CRC Press; 2010. p. 39

[30] Andrews LC, Phillips RL. Laser Beam Propagation through Random Media. London: SPIE Publications; 2005. pp. 121-123

[31] Alimardani M, Toyserkani E, Huissoon JP. A 3D dynamic numerical approach for temperature and thermal stress distributions in multilayer laser solid freeform fabrication process. Optics and Lasers in Engineering. 2007;**45**(12):1115-1130

[32] Lampa C, Kaplan AFH, Powell J, Magnusson C. An analytical thermodynamic model of laser welding. Journal of Physics D: Applied Physics. 1997;**30**(9):1293

[33] Liu H, Sparks T. Modeling and verification of temperature distribution and residual stress in laser aided metal deposition process. Proceedings of the 6th Annual ISC Graduate Research Symposium. 2012;(1):1-7

[34] Oldfield W. A quantitative approach to casting solidification: Freezing of cast iron. Transactions of American Society for Metals. 1966;**59**:945

[35] Fisher DJ, Kurz W. Appendix 7 and 8, Fundamentals of Solidification. Aedermannsdorf: Trans Tech Publication Ltd; 1992. pp. 226-246

[36] Fisher DJ, Kurz W. Appendix 9, Fundamentals of Solidification. Aedermannsdorf: Trans Tech Publication; 1992. pp. 247-260

[37] Chen R, Xu Q, Liu B. A modified cellular automaton model for the quantitative prediction of equiaxed and columnar dendritic growth. Journal of Materials Science and Technology. 2014;**30**(12):1311-1320